JOURNAL OF SPACECRAFT AND ROCKETS
Vol. 48, No. 1, January–February 2011

Overview of the Innovative Space-Based Radar Antenna Technology Program

Steven A. Lane* and Thomas W. Murphey†
U.S. Air Force Research Laboratory, Kirtland Air Force Base, New Mexico 87117
and
Michael Zatman‡
QinetiQ North America, Arlington, Virginia 22202

DOI: 10.2514/1.50252

The U.S. Air Force Research Laboratory and Defense Advanced Research Projects Agency accomplished technology development and demonstration toward a 300 m deployable space antenna under the Innovative Space-Based Radar Antenna Technology program. Risk-reduction activities focused on deployment testing, calibration, structural metrology, and real-time compensation. A 12 m phased-array-fed reflector engineering test unit was tested in a laboratory environment and demonstrated shaping of a single-curved, parabolic-cylinder mesh surface and deployment repeatability. A 12 m engineering test unit using rigidizable-inflatable structural components was also tested, but this approach was more problematic and less robust. Finally, two antenna metrology and compensation engineering test units were tested in a compact range. The results from one were reported. Data showed that the closed-loop system minimized phase error to less than 1/30 of a wavelength, given realistic disturbance inputs.

I. Introduction

IN 2001, the Defense Advanced Research Projects Agency (DARPA) initiated the Innovative Space-Based Radar Antenna Technology (ISAT) program to investigate critical technologies for large, deployable, space radar antenna. These technologies included packaging of large (300 m) linear antennas in conventional launch vehicles, on-orbit antenna deployment and calibration, coherent beamforming and electronic beam-steering, and structural metrology and compensation. The ISAT program matured the state of the art in these areas through concept studies, requirements definition, modeling and simulation, breadboard-level testing and demonstrations, and brassboard-level testing and demonstrations. The program was initially executed by the U.S. Air Force Research Laboratory, Sensors Directorate, and later by the Space Vehicles Directorate.

Much of the early work on ISAT focused on identifying technical requirements, analysis of alternatives, and feasibility studies for an envisioned space radar system architecture referred to as the ISAT Objective System Concept (OSC) [1–12]. OSC studies attempted to identify a space radar architecture that could provide persistent global surveillance and ground moving-target identification and tracking capability. It was desired to obtain tactical-grade radar data, which implied being able to detect and monitor relatively small objects that move slowly (thus, being difficult to discern from background noise). Various concepts to meet these goals were evaluated based on technical feasibility, predicted performance, and system engineering cost models (including development, operation, and disposal). OSC was a challenging mission and studies suggested the need for extremely long linear phased-array antennas (300 m) at high orbits (near 10,000 km, which is considered middle Earth orbit, or MEO). At low Earth orbit (LEO; about 500 km), too many satellites would be required to provide persistent global coverage. At geosynchronous orbits, the antenna length becomes prohibitive large.

After gaining an understanding of technology requirements for the OSC and having assessed the *then-current* state of the art in large deployable antenna technologies, subsequent efforts of the ISAT program focused on developing a low-Earth-orbiting flight demonstration system (FDS). An LEO mission was considered to be necessary and sufficient to reduce risk toward the OSC and would be lower cost than an MEO experiment. The FDS was designed to be traceable to the OSC: essentially, a 100 m version of the 300 m OSC antenna concept. The FDS would provide an on-orbit testbed for 1) studying the behavior and dynamics of the selected large deployable structure concept, 2) verification, validation and refinement of coupled thermoelastic structural and electromechanical models, 3) observing nonlinearities and system variations with time, and 4) hosting a variety of other mission-related, risk-reduction studies. The FDS would greatly enhance our understanding and ability to develop a successful OSC.

There were two alternate concepts being investigated for the FDS and OSC, both of which will be discussed in some detail in this paper. One concept was referred to as an active electronically steerable array (AESA) and the other as a phased-array-fed reflector (PAFR). Both concepts were developed to the Critical Design Review (CDR) program milestone, after which a single design was to be selected for fabrication, launch, and on-orbit experiments. It was required that critical experiment-related (payload) subsystems achieve Technology Readiness Level 5 (TRL-5) by the CDR. For this program, TRL-5 was defined as "component or breadboard validation in a relevant environment." Experiment-related subsystems included 1) the antenna deployment system; 2) the phased-array radar calibration, beam-steering, and control system; and 3) the structural metrology and compensation system. Essentially, this was a component requirement, as it was not cost-effective to accomplish breadboard demonstrations in a simulated space environment.

Remaining spacecraft subsystems (bus, power, radar feed, attitude determination and control, propulsion, command and data handling, etc.) were expected to be at a much higher TRL, leveraging legacy systems and components. Development of the FDS mission also included overall systems engineering, such as defining mission objectives, concept of operations, spacecraft design, manufacturability, assembly, integration, test, launch-vehicle considerations, ground/mission control, experiment data analysis, and end-of-mission disposal.

Received 8 April 2010; revision received 14 July 2010; accepted for publication 17 August 2010.

*Research Aerospace Engineer, Space Vehicles Directorate, 3550 Aberdeen Avenue Southeast. Member AIAA.
†Deployable Structures Lead, Space Vehicles Directorate, 3550 Aberdeen Avenue Southeast. Member AIAA.
‡Technology Solutions Group, 2001 Jefferson Davis Highway, Suite 801.

Ultimately, the DARPA ISAT program ended in 2006 after completion of the CDR, primarily due to lack of support from transition partners. However, many scientific and engineering accomplishments were realized over the course of the effort. The goal of this paper is to document key accomplishments and lessons learned.

This paper presents the design approaches for the ISAT OSC and FDS antenna payload, model and simulation results, and explains how they were intended to operate. This is followed by a discussion of antenna calibration, metrology, and compensation. The two structural deployment engineering test units (ETUs) developed by the ISAT teams to reduce technical risk and demonstrate technical maturity are discussed. One of the contractor metrology and compensation demonstrations is presented and discussed. The authors have attempted to limit the scope of this paper to the research and engineering aspects of the demonstrations as opposed to spacecraft and mission design. Incremental developments and intermediate findings are omitted for brevity.

II. Theory

A. Deployable Radio Detection and Ranging Antenna

Identifying and tracking slow-moving objects requires that the radar system stare at the object over a long period of time (seconds). This would be difficult to do from LEO as a consequence of the relative velocity of the orbiting platform to the Earth's surface. Maintaining a continuous tracking capability would require that multiple LEO satellites be tasked to keep the object in view, requiring a handoff between satellites as one goes over the horizon and the next comes in view of the object [3]. Such handoffs reduce the probability of successfully monitoring an object's track. The relative speed also makes finding a slow-moving vehicle in the radar data difficult, if not impossible. Many of these operational issues are ameliorated by moving the radar platform to a higher orbit. At higher orbits, the radar system would have a longer dwell time. Also, since the field of view of the higher satellite is greater, fewer satellites would be needed to view the entire globe.

Fundamental antenna goals for the OSC were as follows:

1) Operate at *X*-band frequency (10 GHz).

2) Achieve 5 kg/m^2 area density (includes structure, radar hardware, cabling, etc.).

3) Fit into an evolved expendable launch-vehicle (EELV) payload fairing ($\sim$5 m diameter).

4) Achieve a deployed linear array dimension of 300 m.

5) Meet the *stressing requirements* associated with tactical space radar performance [13].

Stressing requirements refers to issues such as beam scanning, operating in a harmful radiation environment, operating for many years on orbit, and maintaining highly coherent beamforming, even when subjected to slewing and thermal-gradient-induced warping. The need for a 300 m aperture was driven largely by going to a higher orbit altitude. Mass and volume constraints were driven by launch-vehicle limits.

Packaging a 300 m deployable phased-array radar antenna into an EELV fairing poses a particularly challenging engineering problem. The structure, which is laden with radar transmit and receive panels, cables, and thermal insulation, must achieve greater than a 60:1 compaction ratio. For the FDS, the structure (larger than 100 m) would be packaged into a smaller payload fairing (4 m diameter), requiring only a 25:1 compaction ratio. The deployed structure would need to be stiff enough to resist mechanical and thermal deflections, yet lightweight enough to meet launch weight requirements.

There has been much work in the area of large deployable structures for space antenna applications [14]. Deployable mesh reflector antennas are commonly used in space communication satellites [15–20]. Mesh reflectors increase the effective area of the antenna, and hence the antenna gain, thereby reducing power requirements. However, management of the deployable mesh reflector adds a complicated subsystem to an already complicated payload. The need for such high compaction ratios spurred interest in innovative, unconventional, space truss technologies such as rigidizable-inflatable (RI) structures [21–28]. Additional discussion regarding design requirements and analysis of large deployable space antenna structures can be found in [29–31].

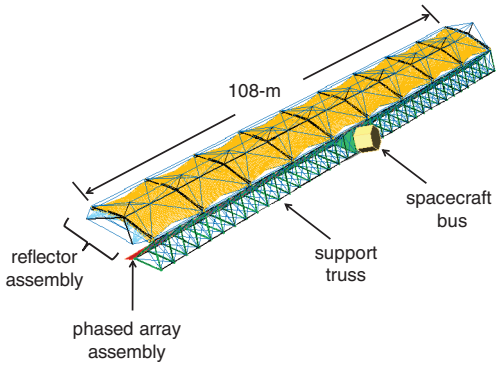

Fig. 1 Illustration of proposed PAFR concept.

Two contractor teams worked on the ISAT program during the final phase of development, each supported by many subcontractors, government research laboratories, and university researchers. One team proposed and developed a PAFR design, which is shown in Fig. 1. This concept used phased-array sources radiating into an unconventional parabolic-cylinder mesh reflector. Figure 1 presents the smaller LEO flight demonstration system (108 m in length). The OSC design was similar, just three times longer. This effort pursued advancements in heritage deployable antenna mechanisms and materials to achieve the necessary compaction ratios and structural performance.

The other team proposed an AESA design, as shown in Fig. 2. This concept was essentially a long truss structure with phased-array radar panels attached along the length. The smaller (104 m) LEO version is shown. Again, the OSC design was similar, just three times longer. Since no reflector was used, the size of the phased-array assembly (feed panels) was greater, as was the weight and power requirements. This team proposed to use rigidizable-inflatable structural components as part of the deployable truss to achieve the necessary compaction.

For both spacecraft designs, the spacecraft bus was positioned at the center of the antenna. The spacecraft bus would provide control of payload functions, manage power, and facilitate attitude control. For each design, the antenna payload (including truss structure, radar panels, sensors, and cabling) was packaged and stacked on top of the spacecraft bus, which was then stacked on top of the launch vehicle, as shown in Fig. 3.

B. Phased-Array-Fed Reflector

1. Geometry

The PAFR design, shown in Fig. 1, was composed of three key subsystems: 1) the main support truss, 2) the mesh reflector assembly, and 3) the phased-array panel assembly. The main support truss was triangular in cross section and was constructed from

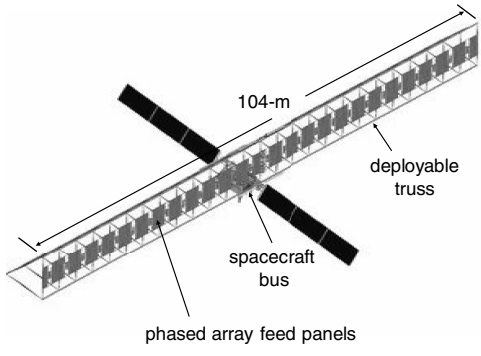

Fig. 2 Illustration of the proposed AESA concept.

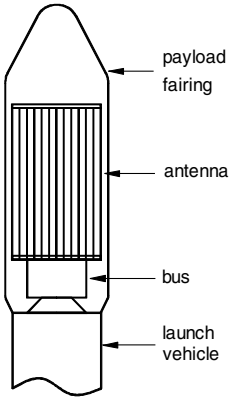

Fig. 3 Schematic of spacecraft stack.

lightweight composite components [32]. A single truss bay is illustrated in Fig. 4. Batten components formed the triangle geometry. Batten length for FDS was 3 m. Thick-walled, folding, longeron components separated batten elements axially along the truss length. Longeron length for FDS was 3 m. Tensioned diagonal components linked alternate batten corners. The FDS main support truss consisted of 36 bays.

The mesh reflector was composed of an elastic mesh, a cord truss to support and shape the mesh, and various tension or compression members (e.g., ribs, deployment mechanisms, articulating linkages, hinges, and latches). For the FDS, the mesh reflector consisted of nine segments, each 12 m in length. The phased-array panel assembly was the third key subsystem. It included the radar transmit and receive modules and was attached along one edge of the main support truss.

2. Model Results

A finite element model of the antenna structure in its stowed configuration was developed and coupled with models of the spacecraft bus and launch vehicle. The estimated total spacecraft wet mass (i.e., with propellant) was less than 5200 kg (the not-to-exceed threshold was 5600 kg). Simulations suggested that the PAFR design met launch-vehicle center-of-gravity requirements and fairing envelope restrictions.

Models of the deployed FDS were used to predict on-orbit structural dynamics and forced responses (from slewing maneuvers or thermally induced deflections). The first structural bending mode occurred at 0.53 Hz. There were a total of 10 non-rigid-body modes below 1.0 Hz and a total of 32 modes below 1.7 Hz. Damping estimates used in simulations were based on heritage flight data of similar components made of similar materials (typically greater than 2% critical damping). Predicted on-orbit loads and stresses were well within design specifications.

Thermal environment simulations were developed for the spacecraft for assumed orbital parameters. Thermal cycling and shadowing effects were analyzed for a given orbital parameter set. Table 1 presents upper and lower temperature bounds for various payload components for a nominal set of mission parameters. These temperature extremes were within allowable component tolerances. The upper mesh temperature of 220°C was consistent with findings given in [17]. Thermal gradients were the greatest source for deployed structure deformations. Predicted on-orbit deformations (mechanical and thermal) were less than 30 mm, which is very small relative to the antenna length.

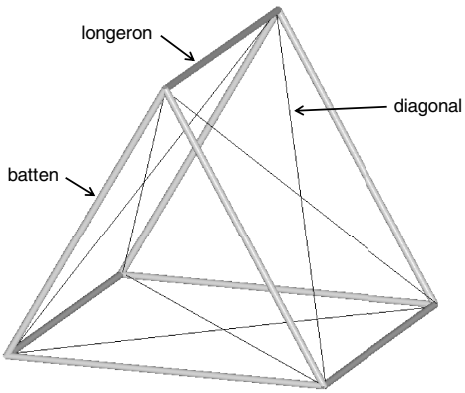

Fig. 4 Single truss bay.

Table 1 Result of thermal analysis for nominal FDS mission parameters

Component	Model predictions	
	T_{min}, °C	T_{max}, °C
Ribs	−75	25
Longerons	−54	46
Battens	−46	36
Diagonals	−100	−4
Mesh	−112	220
Feed panels	−45	25

3. Operation

On-orbit antenna deployment would follow insertion of the spacecraft into the desired orbit and initial spacecraft checkout. After release of launch locks, both the mesh reflector assembly and phased-array feed assembly are rotated off the main support truss from their stowed positions to their deployment-ready position. Next, lead-screw guide rails are unfolded and locked into position to deploy each bay of the main support truss. While oriented along the gravity gradient, antenna bays are sequentially deployed in a balanced fashion from the stowed configuration. The outermost bays are deployed first. Two antenna bays deploy simultaneously, one in each direction. As the main truss is deployed, the mesh reflector assembly is also synchronously deployed. Precise synchronization is required to avoid binding and deployment failure. The phased-array feed panels are attached to and deploy along with the main support truss. Each section of phased-array panels is connected by a composite hinge [33]. These composite hinges, also called *strain-energy hinges*, were also used in the main truss's folding longeron elements.

4. Primary Design Risks

Mesh management was the primary design risk. Mesh management includes packaging and deployment of the reflector assembly so as to avoid the risk of entanglement, snagging, and tearing. The reflector assembly would need to be integrated and stowed to withstand launch and then deployed under a deterministic loading to achieve the necessary deployed surface accuracy. Further discussion of mesh surface accuracy can be found in [34]. Consider that deployment of other payload subsystems (e.g., the main truss and feed-panel assemblies) can be reasonably tested and verified in a laboratory with simulated 0 *g* boundary conditions. However, it is much more difficult to simulate a 0 *g* environment for deployment verification of the reflector subsystem.

C. Active Electronically Steerable Array

1. Geometry

The AESA design shown in Fig. 2 was a 104 m truss with 4 m rigid composite battens forming the triangular cross section of the antenna. Between the battens were 4 m composite, folding, rigidizable-inflatable longerons. Diagonal elements linked alternate batten corners. The truss consisted of 26 4 m bays. Phased-array radar panels were attached along one side of the truss.

2. Rigidizable-Inflatable Components

Figure 5 illustrates a cross section of an RI longeron. Before deployment, while folded (stowed), resistive heaters on the longeron are activated to warm the composite material to a pliable state. Once

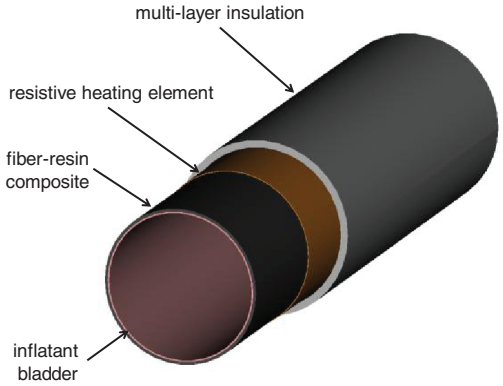

Fig. 5 Cutaway view of an RI composite longeron.

pliable, a gas such as nitrogen is pumped into the bladder within the longeron, causing the longeron to unfold (deploy). Once the longeron is fully deployed, the heaters are turned off and the longeron is allowed to cool. Once cooled below its *glass transition temperature*, the longeron becomes rigid. Multilayer insulating (MLI) material covers the longeron and protects it from solar heating, thus maintaining its temperature below the glass transition temperature for the remainder of the mission.

3. Model Results

The model-based estimate of the total wet mass of AESA spacecraft was less than 4,800 kg. Models of the stowed payload suggested that the AESA design also met launch-vehicle center-of-gravity requirements and fairing envelope restrictions. Models of the deployed FDS indicated that the first bending mode occurred at 0.35 Hz. The first 10 non-rigid-body modes (mostly involving the solar arrays) occurred below 0.5 Hz. Truss damping was estimated by the contractor at 0.3% of critical damping. Predicted on-orbit loads and stresses were within design specifications. Additional information regarding maneuvers and disturbances can be found in [35]. Thermal models and analysis indicated that the maximum on-orbit temperature of the longerons was as high as −20°C. This implied a 10°C margin below the temperature at which the longeron resin begins to soften. The estimated maximum thermal-induced truss deflection was 23 mm, and the maximum slew-induced deflection was 30 mm.

4. Operation

After orbit insertion and spacecraft checkout, the truss is unlocked from its stowed configuration and actuated to its deployment-ready configuration. Guide rails are unfolded and locked into position for sequential antenna bay deployment (one bay in each direction). The outermost antenna bays are deployed first, which starts with heating of the longerons. Once heated to the proper temperature (∼70°C), the longerons are inflated (∼51.7 kPa). While being inflated, the antenna bay is deployed along the three guide rails using a chain-and-sprocket mechanism. The signal and power cables and radar panels deploy with the antenna bay to which they are attached. Synchronization of deployment along each guide rail is critical to avoid binding and deployment failure. Once the bay is deployed (4 m per bay), the heaters on that bay are powered off and that bay is allowed to cool, while the next bay is warmed up. The next bay pushes the previous bay off the guide rails until the antenna is completely deployed. Estimated power required for heating each bay was 400 W. Estimated deployment time for each bay was 10 min.

5. Primary Design Risks

The primary design risk was the rigidizable-inflatable components. Thermal management of the RI longerons required controlled heating and feedback from numerous embedded thermal sensors. On-orbit performance relied on adequate protection from solar heating by the multilayer insulation. Plumbing and control for the inflating gas also added complexity. Laboratory testing proved very difficult and of only limited value, as a result of insufficient traceability to on-orbit conditions.

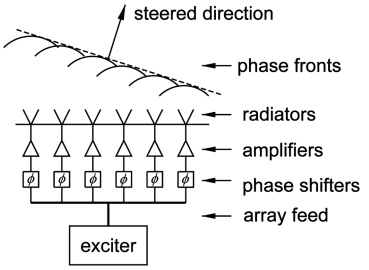

Fig. 6 Illustration of phased-array antenna components.

D. Calibration and Coherent Beamforming

To function properly, an antenna must be calibrated following deployment and frequently during mission life to adapt for changes in the system [36–39]. Figure 6 presents a simplified diagram of a phased-array antenna. The path from the exciter to each radiator can be different, which would impart varying phase shifts on the radiated wave form (for reference, at 10 GHz, one wavelength is about 30 mm). Basic phased-array theory [40–43] demonstrates that paths must be calibrated so that the radiated wave fronts are coherent (in phase). Coherent phase fronts constructively interfere in the far field and allow for high antenna gain in the intended (steered) direction. Conversely, radiated wave forms can be generated out of phase, producing destructive interference, thereby creating nulls [44]. The degree of coherence can be accessed by either measuring the main-lobe or null amplitude. By imparting a controlled phase shift along the antenna, beam-steering (or scanning) can be achieved. Phased-array antennas are typically laboratory-calibrated before leaving their manufacturing facility. It was necessary in the case of ISAT to be able to perform initial and periodic on-orbit calibrations to account for changes in electromechanical performance resulting from deployment, changes in the operating environment, and system variations over time. Additional details on antenna calibration can be found in [45,46].

E. Antenna Metrology and Compensation

Coherence of the antenna can be degraded by relative displacements of the phased arrays along the antenna, and in the case of the PAFR, distortion of the reflector assembly. Antenna distortion can result from bending and twisting as a consequence of thermal gradients or as the result of slewing maneuvers. For an operating wavelength of 30 mm (x band), a 1 mm relative displacement introduces 12° of phase error. To maintain antenna performance, it is necessary to measure antenna distortion and compensate, either structurally or electronically. A two-port formulation of the control problem is presented in Fig. 7. The approach investigated for ISAT was to measure antenna displacements at a fixed number of points along the length of the antenna (called fiducial points) and then adjust the antenna's phase shifters to compensate for the measured displacement.

There are many approaches for antenna metrology, including passive and active approaches. A passive approach might include a center-mounted camera(s) that periodically images antenna geometry and infers displacement from comparisons to prior images

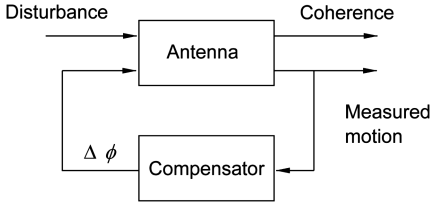

Fig. 7 Metrology and compensation block diagram.

[47–49]. An active approach uses active fiducial points (e.g., light-emitting diodes) or a center-mounted laser ranging unit to measure fiducial movement [50].

The ISAT contractors evaluated various combinations of active and passive metrology systems, considering feasibility, performance, reliability, and cost. Fundamentally, the metrology system should be small (i.e., low mass), unobtrusive, and simple. Complex systems tend to be less robust than simple systems. Systems that require camera(s) mounted to booms that must be deployed orthogonal to the antenna to get a *better view* of the antenna add to the structural dynamics problem. Systems that require active fiducial points consequently require cabling from the metrology system processor to each fiducial point, thus complicating antenna deployment.

From an implementation point of view, one must consider the required number of fiducial points, the necessary sampling rate, and the required accuracy and precision of fiducial measurements. The required number of fiducial points (i.e., spatial sampling) is largely determined by the number of structural modes needed to characterize the structural response and their wavelengths. The temporal sampling rate (i.e., how often the fiducial points needed to be measured) is determined largely by the time scale of the structural response. Metrology accuracy and precision can be traded against complexity and performance. The goal for the ISAT laboratory demonstration was to keep phase error less than $1/20$ of a wavelength (18°), given realistic and traceable disturbances.

The approach presented here was for the PAFR concept, which was considerably more complex than the AESA concept, primarily due to the requirement to measure and compensate for the distortion of the feed, distortion of the reflector, and the relative motion/distortion between them. The proposed metrology system, called a *shallow-angle sensor system*, used a spacecraft-bus-mounted, variable-field-of-view imaging system with closely located laser-emitting diodes that illuminated retroreflecting fiducial points along the main-truss phased-array feed panels and the reflector assembly. Fiducial measurements were input to a Kalman estimator, which was used to *predict ahead* to determine the appropriate phase shifts. Thus, model fidelity was limited by computational speed.

The primary challenge for practical implementation is calibrating the metrology system once the antenna has been deployed on orbit. Assuming that the deployment is successful, there is uncertainty as to the absolute positions of the fiducial points. However, since motion relative to the antenna *calibration state* is all that is required to compensate for antenna distortions and motion, it is sufficient that the fiducial points are near their expected locations (i.e., within the imager's field of view). Calibrating the metrology system requires an on-orbit system-identification process to map motion of the many fiducial points (i.e., pixel movement on the focal plane) to structural motions and then transfer structural motion to phase corrections.

III. Experiments

Three experiments, or demonstrations, are presented in this section. The first is stowing and deployment of the PAFR ETU (half-scale). Next is the stowing and deployment of the AESA ETU, which used rigidizable-inflatable longerons. Finally, metrology and compensation of a phased-array and reflector system is presented.

A. Phased-Array-Fed Reflector Engineering Test Unit

The PAFR ETU consisted of four main-truss bays (1.5 m longerons and 1.5 m battens) with an attached 6 m mesh reflector and multiple phased-array feed-panel *simulators*. Component and subsystem tests were performed before integrated system tests to identify potential design and operation issues. Mechanisms (hinges, latches, actuators) were tested multiple times, often at operational temperatures (−30 to 42°C), to compare measured performance to model simulations.

The composite strain-energy hinges behaved like a tape-spring joint and provided considerable *snap-through* force. Tests were performed on damped versions of the composite hinge, but loads tended to be less deterministic and there was no substantial benefit to using the damped version of the hinge. Figure 8 shows the composite hinge during deployment of the radar feed-panel simulators.

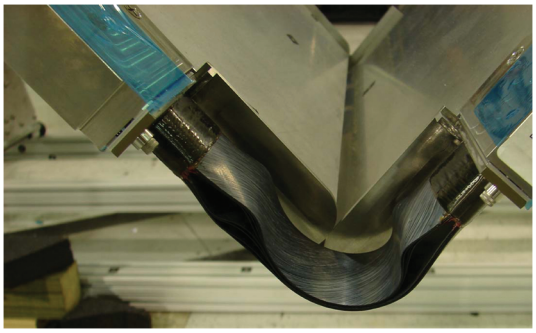

Fig. 8 Composite strain-energy hinge between radar panel simulators (mid-deployment).

Two key subsystems were the main-truss assembly and the reflector assembly. Figure 9 shows the main-truss assembly in its stowed configuration, without the reflector or phased-array panels attached. The motor-actuated drive-belts and the folded lead-screw guide rails are indicated. The deployment procedure for the ETU was traceable to the on-orbit deployment procedure. Once the lead-screw guide rails were unfolded and locked, each triangular-shaped batten was sequentially engaged. As the lead screws rotated, each batten was forced outward from its stowed position. Composite hinges locked the folded composite longerons into position. Each bay (including batten, longerons, and diagonals) was fully formed on the lead screws before being disengaged from the guide rails. This ensured that the sections were fully locked before separating from the actuating mechanism.

Achieving the required surface accuracy of the single-curved mesh reflector was a significant accomplishment. The first task was to assemble and align the support and deployment structure. Once the structure was aligned, the cord truss and the mesh surface were installed. The reflector assembly was laid out horizontally. Photogrammetry was used to assess alignment and surface shape. Adjustments were made to the reflector assembly based on comparison of model predictions to the photogrammetry measurements. After only three iterations, the root-mean-square error in the mesh surface shape was less than 1 mm. This task validated both the models and the design of the support structure and cord truss.

The reflector assembly and phased-array panel assembly were integrated onto the main truss. Figure 10 shows the integrated ETU in a partially stowed configuration, with key subsystems indicated. Initially, three rib-deployment cycles were completed to evaluate structural cord stowage and counterbalancing (see Fig. 11). Gravity offloading was used to reduce binding on the deployment mechanisms. Following rib-deployment testing, the reflector and main

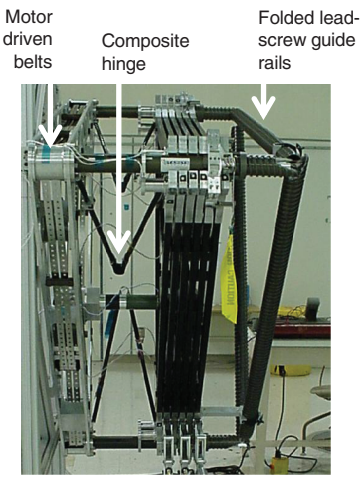

Fig. 9 Stowed PAFR main-truss assembly.

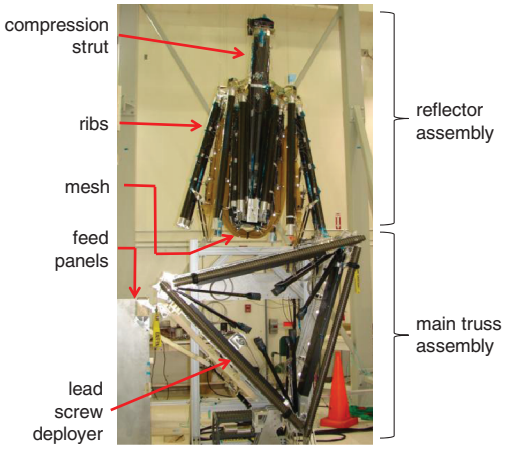

Fig. 10 Stowed PAFR ETU.

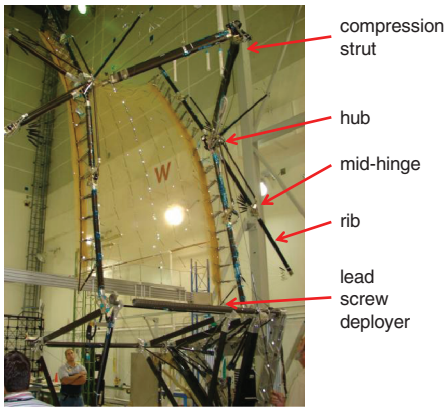

Fig. 11 Partially deployed PAFR ETU.

truss were fully extended to verify operation and mesh management. Then three partial axial stows and deployments were completed of the last 2.5 m to verify mesh management and deployment. Finally, three full axial stows and deployments were completed. The fully deployed ETU is shown in Fig. 12. Retroreflector targets in the mesh reflector from earlier photogrammetry tests can be seen. Along the bottom of Fig. 12, one can observe the main truss and the deployed feed-panel simulators.

For the integrated system tests, control software was more diagnostic and less autonomous than would be used on the actual flight system. Numerous sensors were also incorporated for diagnostic

Fig. 12 Fully deployed PAFR ETU.

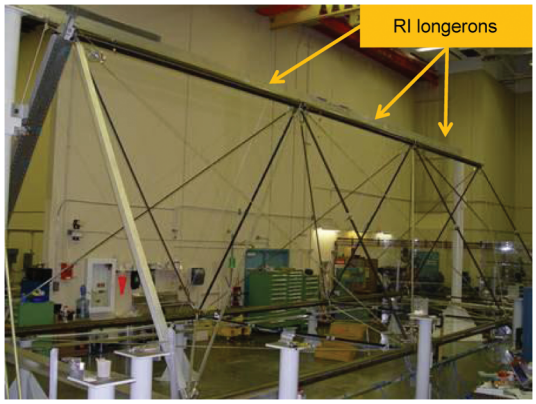

Fig. 13 A 12 m AESA ETU before folding and deployment tests.

purposes. Strain gages attached to the ribs were monitored to verify that loads were consistent with model predictions. Strain gage measurements followed predicted trends, except above 80% of deployment, where the measured strains were lower than predicted. The primary cause was believed to be misalignment between the trusses and rib hubs and possible differences in synchronization geometry.

Test measurements suggested modifications were required to the locking mechanisms to provide more locking force to offset larger-than-expected loads from the tensioned cord truss supporting the mesh reflector. Adjustments were also required to the gravity-offloading system to adapt to the moving center of gravity during deployment. These adjustments improved the overall motor loads during deployment (*improve* means that the measured loads corresponded more with the predicted loads). Synchronized rib deployment, midhinge latching, and mesh and cord management all performed as designed. Mesh management was iteratively refined to reduce snag potential. Although photogrammetry was used on earlier tests of the reflector to verify surface accuracy, no photogrammetry measurements were taken of the (vertical) integrated system, since gravity sag negated the value of such measurements.

B. Active Electronically Steerable Array Engineering Test Unit

The AESA structural ETU consisted of a full-scale 12 m section, which was composed of three 4 m bays. Figure 13 shows the assembled ETU before application of the MLI. Longeron diameter was 12.7 cm. Traditional composites tubes were used for the batten elements. Dry graphite fibers were used for tension diagonal elements. *Nodes* between bays included pressure valves to control the flow of nitrogen for inflating, thermal sensors to control longeron heating, and assemblies to engage the deployment rails. Because of the size of the ETU, it was not feasible to deploy it under spacelike thermal-vacuum conditions. However, individual components were tested (verified) under thermal vacuum, including longeron deployment.

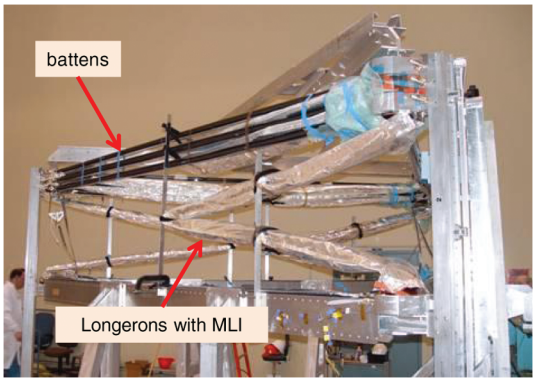

Fig. 14 Stowed configuration of AESA ETU.

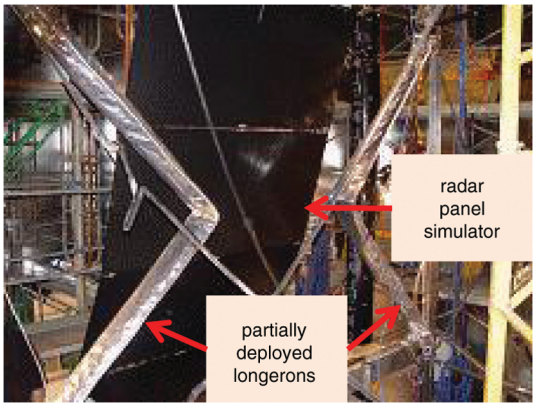

Fig. 15 Partial deployment of AESA ETU with panel mass simulator.

Fig. 17 Metrology and compensation test hardware.

Once the truss was assembled and MLI was applied to the longerons, the longerons were folded so that the truss was in its stowed configuration, as shown in Fig. 14. The stowed truss was integrated with the deployment mechanism, which included guide rails and synchronized, motor-driven, chain deployment mechanisms. A thermally isolated test enclosure was constructed to encapsulate the entire ETU so that the truss could be cooled (postdeployment) to allow stiffness measurements for model validation. The ETU was placed in the test enclosure and integrated with a gravity-offloading system. It was planned that the ETU would be deployed vertically (upward). A deployable radar panel mass simulator was installed onto the third bay to replicate deployment dynamics.

To deploy the longerons, the composite material needed to be heated to approximately 70°C before N_2 was pumped into them. However, MLI was a poor insulator in the laboratory environment due to convective heat transfer created by the surrounding air. Consequently, thermal management for the integrated system deployment process was a challenge. Additional longeron insulation and secondary heating sources were required to achieve the necessary temperature. Near the aluminum end fittings, heat was conducted away from the composite material, which resulted in uneven heating. Sides of the longerons exposed to the air achieved lower temperatures than sides of the longerons facing other longerons (due to folding). During deployment, several thermocouples were damaged, resulting in localized overheating of the composite material. During deployment of the second bay, one of the longerons failed to inflate as a result of a leak created by localized overheating. There were also synchronization problems encountered that encumbered the ETU's deployment. Figure 15 shows partial deployment of the third and final truss bay with the attached radar panel mass simulator. Restowing and redeployment of the AESA ETU were not attempted.

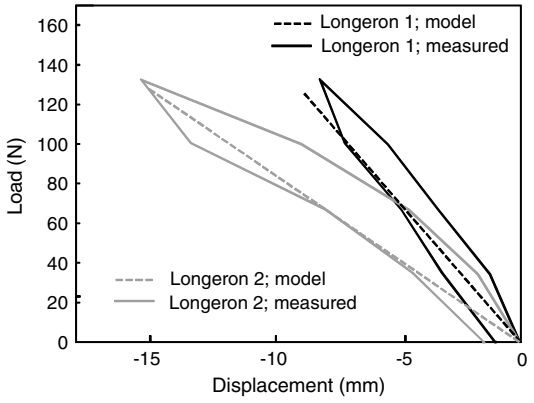

Fig. 16 Force versus displacement measurements of the AESA ETU at ambient conditions.

Once deployed, loads were applied laterally at the top of the truss, and the resulting deflections were measured. Measurements were compared to a rudimentary model of the 12 m truss. Only static tests were conducted (no dynamic or modal tests). Tests were conducted at ambient temperature and at −20°C. Figure 16 presents measured displacement data compared to model predictions for two longerons loaded in a single direction at ambient test conditions. Note that longerons are able to carry load above the glass transition temperature, although there is some performance degradation. Also note that pressurized N_2 was contained within the longerons. Test data showed the response of the AESA ETU to be nonlinear (i.e., the slope of the displacement varied with applied load amplitude). However, the contractor believed that much of the nonlinearity resulted from the tension diagonals as opposed to the RI longerons. Additionally, the data exhibited a hysteresis effect. Similar results were measured when the load was applied in an orthogonal direction. Data from cold measurements (not shown) exhibited similar hysteresis, but diverged slightly more from model predictions.

C. Metrology and Compensation Experiment

The goal of the metrology and compensation experiment was to demonstrate structural metrology and closed-loop control to maintain transmit coherence, given representative structural deformations. Figure 17 presents the testbed, which included a composite reflector, *x*-band phased-array feed panel, and numerous retroreflective metrology fiducial points. A composite reflector (3 × 1.6 m) was used instead of a mesh reflector to allow simulation of distortion shapes predicted for the FDS, without introducing higher spatial frequency distortion shapes that were not traceable to the FDS. Four deformation (disturbance) modes were produced by motors attached to the antenna support structure: 1) reflector and feed-panel translation (rigid-body mode), 2) reflector azimuth rotation (rigid-body mode), 3) reflector elevation rotation (rigid-body mode), and 4) reflector twisting (a non-rigid-body mode simulating surface distortion, which was accomplished by translating each of the four corners only). The feed panel consisted of 192 radiating elements and was stationary during all tests. Tests were conducted in a compact range, which provided an anechoic environment at *x*-band and simulated/enabled far-field measurements. The compact-range receive antenna (not shown) measured the

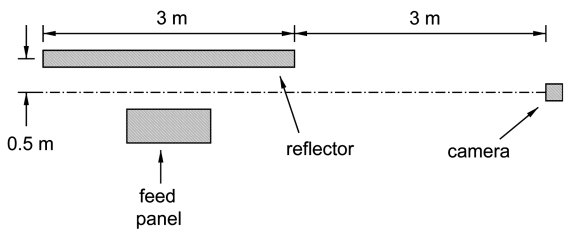

Fig. 18 Layout of metrology camera relative to reflector and feed array.

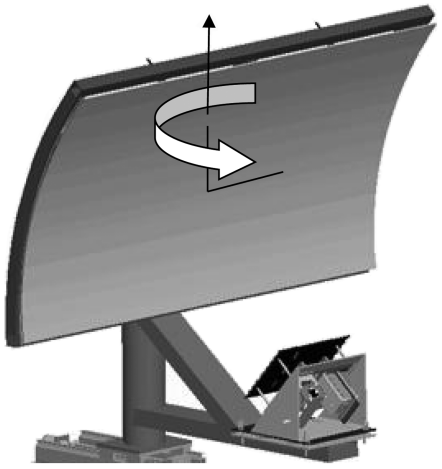

Fig. 19 Illustration of reflector rotation.

transmitted signal from the feed panel. Amplitude and phase were measured by an Agilent 8530 pulse receiver.

The metrology system consisted of an imaging camera, passive 6 mm corner cube reflectors (nine on the reflector, four on the phased-array feed panel), and laser diode illuminators. The camera and illuminators were mounted to the wall within the compact range, approximately 4.5 m to the right of the reflector's vertical center line (see Fig. 18). Metrology processing consisted of centroiding the fiducial points and then performing a two-dimensional (2-D) to three-dimensional (3-D) transformation. Photogrammetry was used a priori to provide model inputs for the 2-D to 3-D transformations for the various types of distortions. Accuracy of the metrology system was 0.4 mm out of plane (normal to the reflector or feed-panel surface) and 1 mm in plane. Outputs from the metrology system were input to the Kalman estimator, which predicted the antenna's state (i.e., relative position and shape of the reflector and phased-array feed) at the next sample time. This was used to adapt the phase shifters (of the a priori calibrated antenna) to minimize phase error.

Initial tests included compensation for static deformations (translation, rotation, twisting), which validated the metrology and compensation system. The radiated far-field pattern was measured over a range of azimuth angles with all transmit elements radiating in phase, which was denoted as the summation measurement. Additionally, measurements were made with half of the radiating elements set out of phase, which produced a null on boresight (0°) and was denoted as the difference measurement.

Next, open-loop and closed-loop tests were conducted using time-varying deformations to demonstrate real-time metrology and compensation. For these tests, the amplitude (or phase) of the transmitted signal on boresight was measured as a function of time. The amplitude and frequency of the disturbances were defined to include the amplitude and frequency predicted for the PAFR FDS.

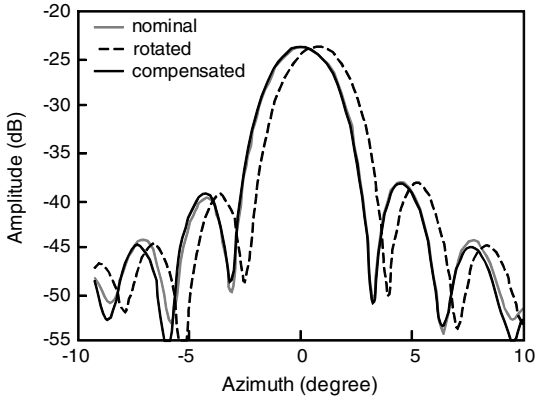

Fig. 20 Static deflection results; summation.

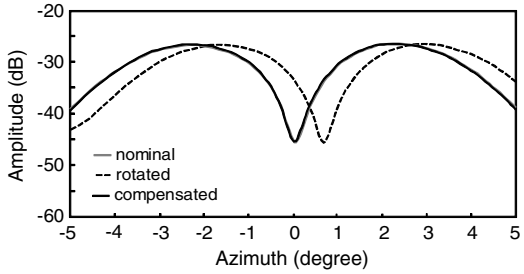

Fig. 21 Static deflection results; difference.

The requirement was to demonstrate real-time control of phase error to less than 1/20 of a wavelength (i.e., 18°).

1. *Static Test Results*

Static test cases included reflector translation (±10 mm), reflector azimuth rotation (±0.6°), reflector elevation rotation (±0.6°), and reflector twist (±6.5 mm translation of opposite corners). Reflector azimuth rotation is illustrated in Fig. 19. The nominal (calibrated) antenna pattern is shown in Fig. 20. This resulted from the summation of all transmitters radiating in phase. The boresight amplitude was −24 dB (normalized; no physical units). After the antenna was rotated 0.6°, the boresight amplitude dropped by about 0.7 dB as the entire pattern shifted to the right. With the metrology and compensation system, the pattern was corrected. The effect on coherence was more pronounced in Fig. 21, which presents the difference pattern. The amplitude on boresight changed from −45 to −34 dB, an 11 dB increase.

Reflector twist is illustrated in Fig. 22. Opposing corners were translated 6.5 mm in the direction indicated. The normalized radiation pattern is given in Fig. 23 and indicates a shift to the left. The difference measurement is given in Fig. 24 and indicates a changed in the null amplitude in addition to the shift. The metrology and compensation system was able to correct for the shift, although the null amplitude was about 5 dB greater than the initial value, which shows that the calibration was better predistortion than postdistortion. Results for translation and rotation in elevation were similar, showing that the metrology and compensation system could correct for static deformations.

2. *Dynamic Test Results*

The first dynamic deformation was ±10 mm translation of the antenna structure, which produced approximately 225° of phase shift. The frequency of the oscillation was 0.04 Hz. Translation does not cause an appreciable effect on the transmitted amplitude. The open- and closed-loop phase responses are shown in Fig. 25. The controller was turned on at about 28 s and was able to measure and compensate for reflector motion in real time. Phase variation was reduced to approximately ±11.3°, which is about 1/30 of a wavelength.

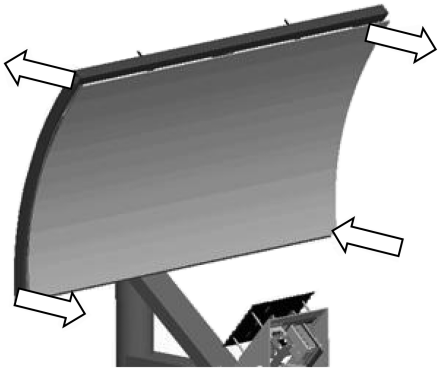

Fig. 22 Illustration of reflector twist.

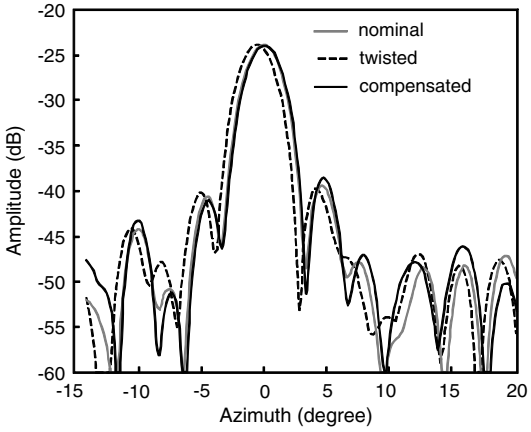

Fig. 23 Static deflection results; twist mode; summation.

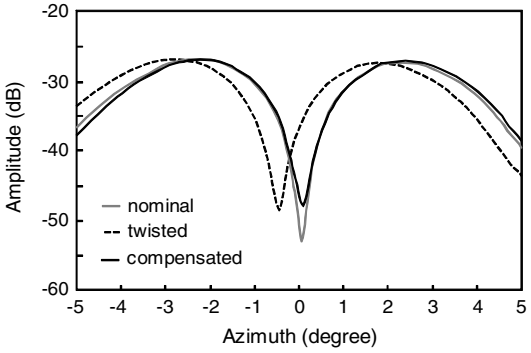

Fig. 24 Static deflection results; twist mode; difference.

The measured open- and closed-loop results for azimuth rotation are presented in Fig. 26. The amplitude of the rotation was $\pm 0.6°$, and the frequency was 0.04 Hz. The amplitude of the difference measurement (null depth) is given in Fig. 26. The metrology and control system was engaged at about 20 s and successfully compensated for the rotation, maintaining the amplitude at about -42.5 ± 2.5 dB, which is close to the nominal value given in Fig. 21.

The final test combined ± 10 mm translation (0.06 Hz), $\pm 1°$ azimuth rotation (0.1 Hz), and ± 12 mm twist (0.08 Hz). The measured phase response is shown in Fig. 27, which started with the controller active. The controller was turned off at about 60 s, at which the phase error became about $\pm 130°$. The controller was turned on at about 120 s, and the phase error was reduced to a root-mean-square value of 6.7°, which is approximately $1/50$ of a wavelength (the root mean square was computed from 120 to 500 s).

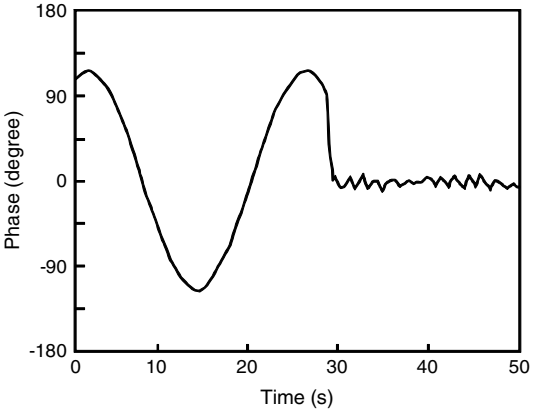

Fig. 25 Open- and closed-loop compensation; reflector translation.

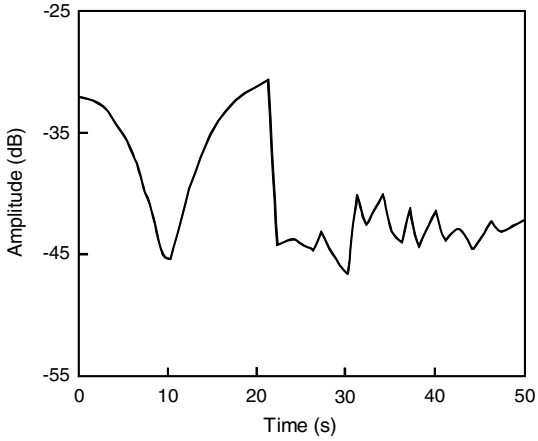

Fig. 26 Open- and closed-loop compensation; reflector azimuth rotation.

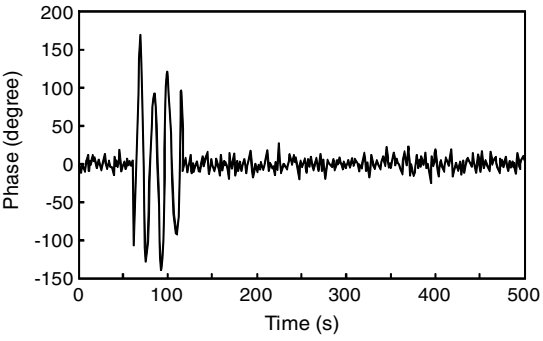

Fig. 27 Open- and closed-loop compensation; reflector translation, rotation, and twist.

IV. Conclusions

This effort accomplished significant research and development related to large deployable structures for space antennas and on-orbit structural metrology and compensation of such structures. This paper presented two structural deployment engineering test units developed by the ISAT contractor teams and one antenna metrology and compensation demonstration. Qualitative and quantitative results from the laboratory demonstrations were presented, as well as primary risks and technology challenges.

Developing and testing a scaled ETU for the PAFR in a laboratory environment was difficult. Thermal deformation testing in a thermal-vacuum environment was not feasible due to the associated costs and complexity. Subsystem and integrated system testing identified potential deployment issues and enabled some degree of model validation. The PAFR ETU was successfully stowed and deployed multiple times.

Deployment and limited testing of the AESA ETU was accomplished, but only after overcoming many technical challenges, most of which resulted from the rigidizable-inflatable composite components. It is not clear that RI technology offers any benefits that would offset the technical risks. Deployment repeatability and model validation were not accomplished. Additional development of the RI technology is needed before it can be shown that it would be suitable for this mission.

Initial calibration of the PAFR metrology system following integration was a considerable challenge. Once accomplished, the metrology and compensation system was able to correct for a variety of traceable disturbances in real time, exceeding the threshold requirement.

References

[1] Kemerley, R., and Kiss, S., "Advanced Technology for Future Space-Based Antennas," *2000 IEEE MTT-S International Microwave*

Symposium Digest, Vol. 2, Inst. of Electrical and Electronics Engineers, Piscataway, NJ, 2000, pp. 717–720. doi:10.1109/MWSYM.2000.863283

[2] Davis, M. E., "Technology Challenges in Affordable Space Based Radar," *2000 IEEE International RADAR Conference*, Inst. of Electrical and Electronics Engineers, Piscataway, NJ, 2000, pp. 18–23. doi:10.1109/RADAR.2000.851798

[3] Guerci, J., and Jaska, E., "ISAT—Innovative Space-Based Radar Antenna Technology," *IEEE International Symposium on Phased Array Systems and Technology*, Inst. of Electrical and Electronics Engineers, Piscataway, NJ, Oct. 2003, pp. 45–51. doi:10.1109/PAST.2003.1256955

[4] Davis, M., Himed, B., and Zasada, D., "Design of Large Space Based Radar for Multimode Surveillance," *Proceedings of the 2003 IEEE Radar Conference*, Inst. of Electrical and Electronics Engineers, Piscataway, NJ, May 2003, pp. 1–6. doi:10.1109/NRC.2003.1203370.

[5] Jaska, E., "Optimal Power-Aperture Balance," *Proceedings of the 2003 IEEE Radar Conference*, Inst. of Electrical and Electronics Engineers, Piscataway, NJ, May 2003, pp. 203–209. doi:10.1109/NRC.2003.1203402.

[6] Corey, L., and Jaska, E., "Antenna Development at DARPA," *Algorithms for Synthetic Aperture Radar Imagery XI*, edited by Edmund G. Zelnio and Frederick D. Garber, Proceedings of SPIE, Vol. 5427, SPIE, Bellingham, WA, 2004, pp. 29–42. doi:10.1117/12.548761

[7] Freeland, R. E., Helms, R. G., Willis, P. B., Mikulas, M. M., Stuckey, W., Steckel, G., and Watson, J., "Inflatable Space Structures Technology Development for Large Radar Antennas," 55th International Astronautical Congress, Paper 04-I.1.10, Oct. 2004.

[8] Greschik, G., Mikulus, M. M., Helms, R. G., and Freeland, R. E., "Strip Antenna Figure Errors Due to Support Truss Member Length Imperfections," 45th AIAA/ASME/ASCE/AHS/ASC Structures, Structural Dynamics & Materials Conf., AIAA Paper 2004-1601, 2004.

[9] Jones, J., "Ground Moving Target Tracking and Exploitation Performance Measures," *Proceedings of the 12th Annual Workshop on Adaptive Sensor Array Processing*, edited by James, F., MIT Lincoln Kab,, Lexington, MA, Dec. 2004.

[10] Kapfer, R., Krumme, M., and Davis, M., "SBR Sparse Array Performance with Subarray Orientation and Timing Errors," *2006 IEEE Conference on Radar*, Inst. of Electrical and Electronics Engineers, Piscataway, NJ, April 2006. doi:10.1109/RADAR.2006.1631838

[11] Page, D., Himed, B., and Davis, M., "Higher Order Clutter Mitigation in Bistatic Space-Based Radar Systems Using a Knowledge-Aided STAP Approach," *2006 IEEE Conference on Radar*, Inst. of Electrical and Electronics Engineers, Piscataway, NJ, 2006, pp. 459–464. doi:10.1109/RADAR.2006.1631840

[12] Luley, R., Maher, J., Hancock, R., and Davis, M., "End-to-end Modeling and Simulation of GMTI Target Detection from Space," *2006 IEEE Conference on Radar*, Inst. of Electrical and Electronics Engineers, Piscataway, NJ, 2006, pp. 590–597. doi:10.1109/RADAR.2006.1631860

[13] Ryan, J., "Innovative Space-Based Radar Antenna Technology," U.S. Air Force Research Lab., Sensors Directorate, Rept. PRDA 01-013-IFKPA, Rome, NY, Aug. 2001.

[14] Freeland, R. E., Helms, R. G., and Mikulus, M. M., "The Applicability of Past Innovative Concepts to the Technology for New Extremely Large Space Antenna/Telescope Structures," 2006 International Conference on Environmental Systems, Society of Automotive Engineers, Paper 2006-01-2063, Warrendale, PA, 2006.

[15] Freeland, R. E., "Survey of Deployable Antenna Concepts," *Large Space Antenna Systems Technology*, Pt. 1, CP-2269, NASA Langley Research Center, Hampton, VA, 1982, pp. 381–422.

[16] Watanabe, M., Meguro, A., Mitsugi, J., and Tsunoda, H., "Module Composition and Deployment Method on Deployable Modular-Mesh Antenna Structures," *Acta Astronautica*, Vol. 39, No. 7, 1996, pp. 497–505. doi:10.1016/S0094-5765(97)85430-6

[17] Miyasaka, A., "Satellite Mesh Reflector Temperature Measured by Using Fine Thermocouples," *Journal of Thermophysics and Heat Transfer*, Vol. 13, No. 1, 1999, pp. 164–165. doi:10.2514/2.6418

[18] Thompson, M. W., "The AstroMesh Deployable Reflector," *1999 IEEE Antennas and Propagation Society International Symposium*, Vol. 3, Inst. of Electrical and Electronics Engineers, Piscataway, NJ, 1999, pp. 1516–1519. doi:10.1109/APS.1999.838231

[19] Mitsugi, J., Ando, K., Senbokuya, Y., and Meguro, A., "Deployment Analysis of Large Space Antenna Using Flexible Multibody Dynamic Simulation," *Acta Astronautica*, edited by R. Monti, Vol. 47, No. 1, 2000, pp. 19–26. doi:10.1016/S0094-5765(00)00014-X

[20] Murphey, T. W., "Historical Perspectives on the Development of Deployable Reflectors," 50th AIAA/ASME/ASCE/AHS/ASC Structures, Structural Dynamics, and Materials Conf., AIAA Paper 2009-2605, 2009.

[21] Freeland, R., Bilyeu, G., and Veal, G., "Validation of a Unique Concept for a Low Cost Lightweight Space Deployable Antenna Structure," *Acta Astronautica*, Vol. 35, Issues 9–11, May–June 1995, pp. 565–572. doi:10.1016/0094-5765(95)00018-U

[22] Freeland, R., Bilyeu, G., Veal, G., Steiner, M., and Carson, D., "Large Inflatable Deployable Antenna Flight Experiment Results," *Acta Astronautica*, Vol. 41, No. 4, 1997, pp. 267–277. doi:10.1016/S0094-5765(98)00057-5

[23] Freeland, R. E., Bilyeu, G. D., Veal, G. R., and Mikulus, M. M., "Inflatable Deployable Space Structures—Technology Summary," 49th International Astronautical Congress, Paper 98-I.5.01, 1998.

[24] Guidanean, K., and Lichodziejewski, D., "An Inflatable Rigidizable Truss Structure Based on New Sub-Tg Polyurethane Composites," 43rd AIAA/ASME/ASCE/AHS/ASC Structures, Structural Dynamics, and Materials Conf., AIAA Paper 2002-1593, 2002.

[25] Michii, Y., Palisoc, A., Guidanean, K., Veal, G., Derbes, B., and Cassapakis, C., "New Generation of Rigidizable/Inflatable Composite for Space Use," 48th AIAA/ASME/ASCE/AHS/ASC Structures, Structural Dynamics, and Materials Conf., AIAA Paper 2007-1812, 2002.

[26] Williams, B. R., and Agnes, G. S., "Mass Efficiencies for Common Large-Scale Precision Space Structures," 46th AIAA/ASME/ASCE/AHS/ASC Structures, Structural Dynamics & Materials Conf., AIAA Paper 2005-2050, 2005.

[27] Williams, B. R., and Agnes, G. S., "Minimum Mass Design of Large-Scale Space Trusses Subjected to Thermal Gradients," 47th AIAA/ASME/ASCE/AHS/ASC Structures, Structural Dynamics, and Materials Conf., AIAA Paper 2006-1687, 2006.

[28] Murphey T., "Chapter 1: Booms and Trusses," *Recent Advances in Gossamer Spacecraft*, Progress in Astronautics and Aeronautics, Vol. 212, edited by Christopher H. M. Jenkins, AIAA, Reston VA, 2006.

[29] Salehian, A., Cliff, E., and Inman, D., "Continuum Modeling of an Innovative Space-Based Radar Antenna Truss," *Journal of Aerospace Engineering*, Vol. 19, Oct. 2006, pp. 227–240. doi:10.1061/(ASCE)0893-1321(2006)19:4(227)

[30] Jones, T., Bart-Smith, H., Mikulas, M., and Watson, J., "Finite Element Modeling and Analysis of Large Pretensioned Space Structures," *Journal of Spacecraft and Rockets*, Vol. 44, No. 1, 2007, pp. 183–193. doi:10.2514/1.23116

[31] Murphey, T., Cliff, E., and Lane, S., "Matching Space Antenna Deformation Electronic Compensation Strategies to Support Structure Architectures," *IEEE Transactions on Aerospace and Electronic Systems*, Vol. 46, No. 3, July 2010, pp. 1422–1436. doi:10.1109/TAES.2010.5545198

[32] Allen, B., Lenzi, D., and Harvey, T., "Highly Compact Precision Lightweight Deployable Truss Which Accommodates Side Mounted Components," U.S. Patent 6,970,143 B2, 29 Nov. 2005.

[33] Domber, J., Hinkle, J., Peterson, L., and Warren, P., "Dimensional Repeatability of an Elastically Folded Composite Hinge for Deployed Spacecraft Optics," *Journal of Spacecraft and Rockets*, Vol. 39, No. 5, 2002, pp. 646–652. doi:10.2514/2.3877

[34] Mobrem, M., "Methods of Analyzing Surface Accuracy of Large Antenna Structures Due to Manufacturing Tolerances," 44th AIAA/ASME/ASCE/AHS Structures, Structural Dynamics, and Materials Conf., AIAA Paper 2003-1453, 2003.

[35] Liu, J., Bender, D., Chiang, R., Chen, S., and Wang, W., "Innovative SBR Antenna Technology (ISAT) ACS Design," AIAA Guidance, Navigation and Control Conf. and Exhibit, AIAA Paper 2008-7231, 2008.

[36] Srivastava, S., Dantec, P., Hawkins, R., Banik, B., Gray, R., Murnaghan, K., Guertin, G., and Shepherd, N., "RADARSAT-1 Image Quality and Calibration-- Continuing Success in Extended Mission," *Advances in Space Research*, Vol. 32, No. 11, 2003, pp. 2295–2304. doi:10.1016/S0273-1177(03)90557-6

[37] Mailloux, R., *Phased Array Antenna Handbook*, 2nd ed., Artech House, Norwood, MA, 2005, pp. 353–378.

[38] Lenz, R., Schuler, K., Younis, M., and Wiesbeck, W., "TerraSAR-X Active Radar Ground Calibrator System," *IEEE Aerospace and Electronic Systems Magazine*, May 2006, pp. 30–33. doi:10.1109/MAES.2006.1635172

[39] Fenn, A., *Adaptive Antennas and Phased Arrays for Radar and Communications*, Artech House, Norwood, MA, 2008, pp. 204–206.
[40] Demarest, K., *Engineering Electromagnetics*, Prentice–Hall, Upper Saddle River, NJ, 1998, pp. 606–16.
[41] Abid, M., *Spacecraft Sensors*, Wiley, West Sussex, England, U.K., 2005, pp. 230–238.
[42] Mailloux, R., *Phased Array Antenna Handbook*, 2nd ed., Artech House, Norwood, MA, 2005, pp. 1–62.
[43] Fenn, A., *Adaptive Antennas and Phased Arrays for Radar and Communications*, Artech House, Norwood, MA, 2008, pp. 191–214.
[44] Mailloux, R., *Phased Array Antenna Handbook*, 2nd ed., Artech House, Norwood, MA, 2005, p. 11.
[45] Hung, E., "Matrix-Construction Calibration Method for Antenna Array," *IEEE Transactions on Aerospace and Electronic Systems*, Vol. 36, No. 3, 2000, pp. 819–828. doi:10.1109/7.869501
[46] Bhattacharyya, A., *Phased Array Antennas*, Wiley, Hoboken, NJ, 2006, pp. 450–453.
[47] Huang, C., and Chang, T., "Ten Channel Vibration Sensor," *Proceedings of the 1981 Control and Communication Technology in Laser Systems Conference*, Vol. 295, edited by K. Yong, SPIE, Bellingham, WA, 1981, pp. 170–175.
[48] Duren, R., and Liebe, C., "The SRTM Sub-Arcsecond Metrology Camera," *Proceedings of the IEEE Aerospace Conference*, Inst. of Electrical and Electronics Engineers, Piscataway, NJ, 2001, pp. 2037–2046.
[49] Kimura, S., Takeuchi, M., Harima, K., Fukase, Y., Sato, H., Yoshida, T., Miyasaka, A., Noda, H., Sunakawa, K., and Homma, M., "Visual Analysis in a Deployable Antenna Experiment," *IEEE Transactions on Aerospace and Electronic Systems*, Vol. 40, No. 1, 2004, pp. 247–258. doi:10.1109/TAES.2004.1292157
[50] Liebe, C., Abramovici, A., Bartman, R., Chapsky, J., Chapsky, L., Coste, K., and Lam, R., "Optical Metrology System for Radar Phase Correction on Large Flexible Structure," *2008 IEEE Aerospace Conference*, Inst. of Electrical and Electronics Engineers, Piscataway, NJ, 2008, pp. 1–7.

G. Agnes
Associate Editor